Nigerian Journal of Physics (NJP)
ISSN online: 3027-0936
ISSN print: 1595-0611
DOI: https://doi.org/10.62292/njp.v35i3.2026.568
Volume 35(3), September 2026

Magnetic Field Morphology and Star Formation Efficiency in Protostellar Cores: An ALMA Polarimetric Analysis

***[1]Patrick C. Okezuonu, [1]Jemima N. Ogwo, [2]Emenike Nwaokoro, [3]Chinedu O. Dike and [4]Prince O. Orji**

[1]Department of Physics, Abia State University, Uturu, Nigeria.
[2]Department of Industrial Physics, Abia State University, Uturu, Nigeria.
[3]Department of Physics, Alex Ekwueme Federal University, Ndufu-Alike, Nigeria.
[4]Department of Physics and Astronomy, University of Nigeria, Nsukka, Nigeria.

*Corresponding Author's Email: chineduokezuonupatrick@gmail.com

ABSTRACT

We present an observational study of magnetic field structure and star formation efficiency (SFE) in a sample of 26 protostellar cores using dust polarization data obtained with the Atacama Large Millimeter/submillimeter Array. The sample is composed primarily of low-mass star-forming systems, allowing a focused investigation of magnetic regulation at core scales. Magnetic field strengths are estimated using the Davis-Chandrasekhar-Fermi method, while SFE is derived from literature-based gas and stellar mass measurements. The results show that magnetic field strengths span over an order of magnitude, while SFE extends from moderate to high values, with several sources approaching unity. No single monotonic relationship is observed between magnetic field strength and SFE; instead, a structured distribution emerges. Magnetic field morphology plays a significant role in shaping this behavior: hourglass configurations are associated with relatively stronger fields and lower efficiencies, whereas turbulent and non-axisymmetric morphologies extend toward higher SFE values. These findings indicate that, at protostellar core scales, magnetic fields influence but do not uniquely determine star formation efficiency. Instead, SFE reflects the combined effects of magnetic field geometry, turbulence, and localized feedback processes. This study provides observational constraints on the role of magnetic fields in regulating collapse and disk formation in low-mass star-forming environments.

Keywords:
Star formation,
Magnetic fields,
Molecular clouds,
Collapse regulation,
Interstellar medium,
Hub-filament,
Feedback,
Polarization.

INTRODUCTION

Star formation within molecular clouds proceeds through the gravitational collapse of dense cores, where magnetic fields, turbulence, and feedback interact to regulate the efficiency of gas conversion into stars. In low-mass star-forming environments, magnetic fields are thought to influence the collapse process by guiding material inflow, shaping protostellar disks, and regulating angular momentum transport (Crutcher 2012; Li et al. 2014; Bakare et al., 2024). In addition to magnetic effects, variations in gas density have also been proposed as a key determinant of star formation efficiency, with denser regions generally exhibiting enhanced collapse conditions (Okezuonu & Ogwo 2021).

Recent advances in interferometric polarimetry with the Atacama Large Millimeter/submillimeter Array have enabled high-resolution mapping of magnetic field structures in protostellar cores. These observations reveal a diversity of morphologies, including hourglass-shaped fields indicative of magnetically regulated collapse, as well as more disordered configurations suggestive of turbulence-dominated dynamics (Hull et al. 2014; Koch et al. 2018; Liu et al. 2021).

Although individual protostellar systems have been studied in detail, a systematic comparison across a sample of cores is required to establish how magnetic field strength and morphology relate to star formation efficiency (SFE). In this work, we analyze a sample of 26 protostellar cores observed with ALMA and investigate the relationship between magnetic field properties and SFE within a consistent observational framework. By focusing on a homogeneous interferometric dataset, this study isolates the role of magnetic fields at core scales while complementing earlier studies that emphasize the role of density and environmental conditions in shaping star formation efficiency (Okezuonu & Ogwo 2021).

MATERIALS AND METHODS

Observations and Data

Sample Selection

To investigate the relationship between magnetic fields and star-formation efficiency across diverse star-forming environments, we compiled a sample of 26 Galactic star-forming regions selected from published ALMA polarimetric surveys (e.g., Ward-Thompson et al. 2017; Pattle et al. 2017; Hull et al. 2014; Hull & Zhang 2019). The sample was designed to include the 26 low-mass protostellar cores in order to span a broad range of physical conditions and evolutionary environments. Only sources with resolved dust polarization maps of sufficient quality were included, requiring a minimum polarization signal-to-noise ratio of $P/\sigma_P \geq 3$ and adequate spatial sampling to provide at least ten independent polarization vectors across the dense core structure (Hildebrand et al. 2009; Planck Collaboration 2016). This criterion ensures that polarization angle dispersions can be measured reliably for magnetic-field analysis.

In addition to polarization quality requirements, each selected source was required to have corresponding molecular-line observations available in the literature to provide the non-thermal velocity dispersions needed for Davis-Chandrasekhar-Fermi magnetic-field calculations (Davis-Chandrasekhar-Fermi method; Davis 1951; Chandrasekhar & Fermi 1953; Crutcher et al. 2004), as well as published gas mass or dust continuum measurements sufficient for density estimation and star-formation efficiency determination (e.g., Kauffmann et al. 2008; Evans et al. 2009). The final sample spans distances from 125 pc to 1.10 kpc, based on published Gaia-refined parallax distances where available (Gaia mission; Gaia Collaboration 2018), thereby encompassing nearby isolated low-mass protostellar systems such as CB 26 and B335 IRS. These source distances are now explicitly listed in Appendix Table A1. The use of interferometric polarimetric observations ensures that the physical spatial scales probed are confined to dense core and disk-envelope regions, providing a consistent view of magnetic-field structure at protostellar scales (ALMA Partnership et al. 2015; Hull et al. 2014). Because the observations have comparable angular resolution and sensitivity, variations due to beam dilution and large-scale emission filtering are minimized. This observational uniformity allows the derived magnetic-field properties, including field strength and morphology, to be compared across sources within a common physical regime. As a result, the dataset can be treated as a relatively homogeneous sample of protostellar cores, suitable for a controlled investigation of the relationship between magnetic fields and star formation efficiency.

To ensure internal consistency across the sample, all derived physical quantities were evaluated using source-averaged measurements over the characteristic dense core radii reported in the original ALMA studies (e.g., Hull et al. 2014; Koch et al. 2018; Liu et al. 2021). Magnetic-field strengths, gas densities, and velocity dispersions were computed from representative averaged values associated with the dominant polarized emission regions, rather than pixel-scale measurements, thereby reducing the influence of local fluctuations and observational noise. All sources were analysed under a uniform Davis-Chandrasekhar-Fermi (DCF) framework (Davis 1951; Chandrasekhar & Fermi 1953; Ostriker et al. 2001), ensuring methodological consistency across the dataset. Because the sample consists exclusively of low-mass protostellar cores observed with comparable interferometric resolution, the derived parameters reflect similar physical regimes. As a result, the inferred trends are interpreted as intrinsic variations within protostellar core environments, rather than artifacts of differing spatial resolution, density regime, or large-scale environmental diversity.

Classification of Regions

All-star-forming regions in the present sample were classified within the low-mass protostellar regime, consistent with their identification as Class 0/I systems observed at core scales with the ALMA. The selected sources are associated with protostellar objects forming solar-type and intermediate-mass stars, typically characterized by final stellar masses below 8 $M_{\odot}$, following the conventional definition of low-mass star formation (Zinnecker & Yorke 2007; Motte et al. 2018). Because the sample is restricted to low-mass environments, no further subdivision by mass scale is required. Instead, classification focuses on structural morphology, magnetic-field geometry, and feedback activity, which provide the primary physical distinctions among the sources. This approach ensures that all regions are analyzed within a consistent evolutionary and physical regime, allowing meaningful comparison of magnetic field properties and star formation efficiency across protostellar cores.

Structural classification was based on the presence or absence of hub-filament systems identified from published continuum and column-density maps. A region was classified as hub-filament when a centrally condensed hub was connected to two or more converging filamentary structures feeding material into the central core, following the observational framework of Myers (2009) and André et al. (2014). Regions lacking such converging filamentary inflow patterns were classified as non-hub-filament systems.

Feedback activity was classified as present when observational evidence existed for active gas-disrupting processes associated with young stellar objects, following standard observational diagnostics of stellar feedback in star-forming regions (e.g., Arce et al. 2007; Frank et al. 2014; Krumholz et al. 2014; Dale 2015). In low-mass systems, this included bipolar molecular outflows, jets, Herbig–Haro objects, or shocked molecular emission. The full operational criteria adopted for all classifications are summarized in Table 1.

Table 1: Summarizes the operational classification criteria adopted for protostellar cores, focusing on core-scale morphology, filamentary context, and protostellar feedback

S/N	Parameter	Classification	Operational Definition	Example Sources	Literature Basis
1	Mass Scale	Low-Mass	Forms stars with final stellar mass < 8 ($M_\odot$)	CB 26, B335 IRS	Zinnecker & Yorke (2007)
2	Structure	Hub–Filament Present	Central hub connected to ≥ 2 converging filaments	L1448 IRS 2, NGC 1333 IRAS 4A	André et al. (2014)
3	Structure	No Hub–Filament	Isolated or weak filamentary association	CB 26, L1165	André et al. (2014)
4	Morphology	Hourglass	Symmetric inward-curved magnetic field toward collapse axis	NGC 1333 IRAS 4A	Hull et al. (2017)
5	Morphology	Pinched	Partial inward bending without full symmetry	Ser-emb 6	Koch et al. (2018)
6	Morphology	Turbulent	Disordered or irregular polarization orientations	HH 211 mm, SVS 13	Pattle et al. (2022)
7	Feedback	Present	Bipolar outflows, jets, or shock signatures	HH 211 mm, L1157	Arce et al. (2007); Frank et al. (2014)
8	Feedback	Absent	No clear outflow or jet activity detected	CB 26, CB 244	Bally (2016)

Magnetic Field Morphology Classification

Magnetic-field morphology was classified from polarization vector maps into three categories: hourglass, pinched, and turbulent, following commonly adopted observational classifications in submillimetre polarimetric studies (Hull et al. 2017; Koch et al. 2018; Pattle et al. 2022). Hourglass morphology was assigned when polarization vectors exhibited symmetric inward curvature toward a central collapse axis on both sides of the core, consistent with magnetically regulated gravitational collapse (e.g., Girart et al. 2006; Stephens et al. 2013). Pinched morphology was assigned when field lines showed partial inward bending toward the dense core but lacked full bilateral symmetry or complete hourglass convergence, representing an intermediate or partially developed collapse geometry (Koch et al. 2012; Hull et al. 2017).

Turbulent morphology was assigned when polarization vectors displayed irregular or highly disordered orientations with no coherent large-scale curvature pattern, typically associated with significant angular dispersion in polarization angles and dynamically disordered magnetic-field structures (Planck Collaboration 2016; Pattle et al. 2017).

Regions exhibiting predominantly straight or linear magnetic fields without measurable inward curvature were grouped with the non-hourglass category, as such configurations indicate the absence of strong collapse-induced magnetic pinching rather than fully developed turbulent disorder. This avoids introducing an additional underpopulated morphology class while preserving the distinction between organized and collapse-modified magnetic-field geometries. Classification was performed by visual inspection of the published polarization maps, with morphological assignments guided by the dominant large-scale field structure reported in the original observational studies (Hull et al. 2017; Koch et al. 2018; Pattle et al. 2022). In cases where morphology classification was ambiguous, the classification adopted in the original source publication was retained.

Derived Physical Parameters

Star Formation Efficiency

The star-formation efficiency (SFE) for each region was computed using

$$SFE = \frac{\mathrm{M}_\star}{\mathrm{M}_\star + \mathrm{M}_{\mathrm{gas}}} \qquad (1)$$

where $\mathrm{M}_\star$ is the stellar mass associated with the star-forming region and $\mathrm{M}_{\mathrm{gas}}$ is the molecular gas mass. The adopted gas and stellar masses, together with their source-by-source literature origin, are listed in Appendix Table A1.

The gas masses adopted in this study were compiled from published observational catalogs and source-specific literature values retrieved primarily through the VizieR astronomical database (Ochsenbein et al. 2000) together with the original ALMA source publications associated with each region (Hull et al. 2014; Pattle et al. 2022). These published gas masses were originally derived in the respective observational studies from dust continuum or molecular-line analyses using source-specific assumptions for dust temperature, dust opacity, emissivity index, and gas-to-dust ratio appropriate to each observing wavelength and environment (Hildebrand 1983; Kauffmann et al. 2008; André et al. 2014). Because these physical assumptions vary between source studies, the present work adopts the published gas masses directly rather than recalculating them independently.

The stellar masses were similarly obtained from published protostellar catalogs and source literature associated with each region. For these low-mass protostellar systems, stellar masses correspond to embedded protostars reported in ALMA source studies (Hull et al. 2014; Liu et al. 2021).

Table 2: The literature provenance of the gas and stellar masses used in the SFE calculations while their gas and stellar masses are listed in appendix Table A1

S/N	Source Type	Gas Mass Source	Stellar Mass Source	Typical Data Origin	Example References
1	Low-Mass Protostars	Published ALMA continuum mass estimates	Protostellar catalog literature values	ALMA archive studies	Hull et al. (2014), Liu et al. (2021)
2	Hub–Filament Systems	Literature continuum clump masses	Source-specific protostellar mass estimates	ALMA + literature compiled values	André et al. (2014), Motte et al. (2018)
3	Feedback Regions	Published dust continuum masses	Literature-derived stellar masses	ALMA catalogs	Hull et al. (2014), Pattle et al. (2022)

Magnetic Field Strength

The plane-of-sky magnetic-field strength, B_{pos}, was estimated for each region using the Davis–Chandrasekhar–Fermi (DCF) method (Davis 1951; Chandrasekhar & Fermi 1953),

$$B_{pos} = Q\sqrt{4\pi\rho}\,\frac{\sigma_v}{\sigma_\phi}, \qquad (2)$$

where Q is a dimensionless correction factor, ρ is the gas mass density, σ_v is the one-dimensional non-thermal velocity dispersion, and σ_ϕ is the dispersion in polarization position angle expressed in radians. A value of $Q = 0.5$ was adopted following the calibration of Ostriker et al. (2001) for turbulent magnetized clouds with modest angular dispersions.

The gas densities, velocity dispersions, and magnetic-field angle dispersions used in the DCF calculations were compiled on a source-by-source basis from the same observational datasets used to define the physical properties of the sample, primarily drawn from the ALMA polarimetric studies of Galactic star-forming regions (Hull et al., 2014; Ward-Thompson et al., 2017; Pattle et al., 2017). Gas density was estimated from the adopted gas mass and effective source volume following standard dense-core volume assumptions (Crutcher et al., 2004; Liu et al., 2021). For compact protostellar cores, an approximately spherical geometry was assumed $V = (4/3)\pi R^3$, while for elongated clump or filamentary structures a cylindrical approximation $V = \pi R^2 L$ was adopted where this better matched the morphology reported in the original source publication (Pattle & Fissel, 2019). In all cases, the characteristic radius R was taken from the dominant polarized emitting structure identified in the corresponding ALMA study (Hull et al., 2014; Koch et al., 2018).

Velocity dispersions were adopted from published molecular-line observations associated as closely as possible with the dense core structures traced by the polarization maps. Because the sample is drawn from multiple ALMA studies of low-mass protostellar systems, the specific molecular tracers are not identical for all sources; commonly used tracers include CO, $C^{18}O$, N_2H^+, and HCO^+, depending on data availability in the original observations (Hull et al. 2014; Soam et al. 2018; Liu et al. 2021).

For each source, the adopted velocity dispersions, together with the corresponding gas densities and polarization angle dispersions, are listed in Appendix Table A2. Where non-thermal velocity dispersions were explicitly reported in the original studies, those values were used directly. Otherwise, published linewidths were adopted as reported, without re-deriving thermal corrections. Although the observational parameters are derived from a range of ALMA datasets, all measurements probe comparable dense core environments. The use of different molecular tracers therefore reflects observational availability rather than fundamental differences in physical regime. This tracer variation is retained as a source of systematic uncertainty, but does not compromise the overall consistency of the sample for comparative analysis of magnetic field properties in low-mass protostellar cores.

The polarization angle dispersion σ_ϕ was estimated from the spread of polarization position angles measured across the dominant polarized structure in each source, following the Davis–Chandrasekhar–Fermi formalism (Davis, 1951; Chandrasekhar & Fermi, 1953). In the present compilation, no additional structure-function correction for large-scale ordered magnetic-field variation was applied beyond the measurements already reported in the original source studies. Accordingly, no post-processing correction following the Hildebrand–Houde formalism was imposed (Hildebrand et al., 2009; Houde et al., 2009). The resulting σ_ϕ values should therefore be interpreted as first-order DCF estimates suitable for comparative inter-source analysis rather than precision absolute magnetic-field determinations (Pattle et al., 2017; Pattle et al., 2023).

Uncertainties in the DCF magnetic-field strengths are dominated by contributions from gas density, velocity dispersion, polarization angle dispersion, and projection effects. Consistent with previous observational studies, the derived magnetic-field strengths are reported to no more than two significant figures and should be regarded as uncertain to at least a factor of a few (e.g., Liu et al. 2021). The full set of DCF input parameters, including gas density, velocity dispersion, and polarization angle dispersion (in both degrees and radians), together with the resulting magnetic-field estimates is provided in Appendix Table A2. Sources with angular dispersions exceeding the small-angle validity regime of the DCF method are retained for comparison but are interpreted with caution, and their reliability is explicitly indicated in the table.

Magnetic Field Morphology Classification

Magnetic-field morphology for each star-forming region was classified using the morphological criteria adopted in this study and applied to the published ALMA polarization vector maps compiled for the analysis. The plane-of-sky magnetic-field orientations were examined relative to the dust continuum emission structure, and each region was assigned to one dominant morphology category-hourglass, pinched, or turbulent-based on the prevailing large-scale polarization pattern visible in the original observational maps (Hull et al., 2017; Koch et al., 2018; Pattle et al., 2022).

Classification was performed by visual inspection of the polarization vector distributions, emphasizing the symmetry, curvature, and coherence of the magnetic-field geometry across each mapped core or clump. In cases where the morphology was ambiguous, the dominant interpretation reported in the original source publication was adopted in order to maintain consistency with the primary observational analyses (Hull et al., 2014; Ward-Thompson et al., 2017). This procedure ensures that the morphological grouping used in the comparative statistical analysis remains directly anchored to the published polarimetric datasets rather than subjective reinterpretation.

Classification Framework

To enable systematic comparative analysis within a homogeneous protostellar core sample, each region was assigned to a composite classification group defined by three observational parameters: (1) structural context, based on the presence or absence of filamentary or locally converging gas structures surrounding the core; (2) magnetic-field morphology, classified as hourglass, pinched, or turbulence as defined in Section 2.3; and (3) feedback activity, classified as present or absent based on observational evidence of protostellar outflows or jets.

The structural classification is based on whether the core is embedded within a filamentary environment or exhibits localized gas inflow structures, as identified from continuum and column-density maps (Myers 2009; André et al. 2014). In the context of low-mass star formation, such structures are interpreted as channels for mass accretion onto protostellar cores rather than large-scale hub–filament systems associated with clustered massive star formation.

Feedback activity is defined by the presence of protostellar outflows, jets, or shocked gas emission, which are commonly observed in Class 0/I systems and represent the dominant form of feedback at core scales (Arce et al. 2007; Frank et al. 2014; Bally 2016). Radiative and ionization-driven feedback processes associated with high-mass stars are not considered in this classification, as they are not relevant to the present low-mass protostellar sample.

This classification framework defines physically meaningful subclasses within a consistent core-scale regime, allowing magnetic-field strength, morphology, and star formation efficiency to be compared across protostellar environments with differing structural context and feedback activity. The resulting scheme enables a focused assessment of how magnetic regulation varies among embedded cores, without invoking large-scale environmental effects associated with high-mass star formation.

RESULTS AND DISCUSSION

Source Classification and Sample Distribution

The ALMA sample used in this study consists of 26 protostellar cores classified according to their structural context and feedback activity, as defined in Section 3.4. The distribution of sources across classification groups is summarized in Table 3 and illustrated in Figure 1.

Table 3: Distribution of ALMA Protostellar Core Classification Groups

Classification Group	Number of Sources
Filamentary + Feedback	13
Feedback Only	7
Isolated Core (No Filament, No Feedback)	3
Filamentary Only	3
Total	26

The sample is dominated by systems exhibiting both filamentary structure and active protostellar feedback, comprising 13 sources. These objects represent embedded cores in dynamically evolving environments where gas inflow and outflow processes occur simultaneously. A further 7 sources show evidence of feedback activity without clear filamentary association, indicating that protostellar evolution and gas ejection processes can proceed in more localized or less structured environments. Only a small fraction of the sample consists of isolated cores lacking both filamentary structure and feedback (3 sources), while 3 sources exhibit filamentary structure without clear evidence of active feedback. This distribution indicates that most protostellar cores in the ALMA sample are embedded within structured and dynamically active environments, rather than evolving in isolation.

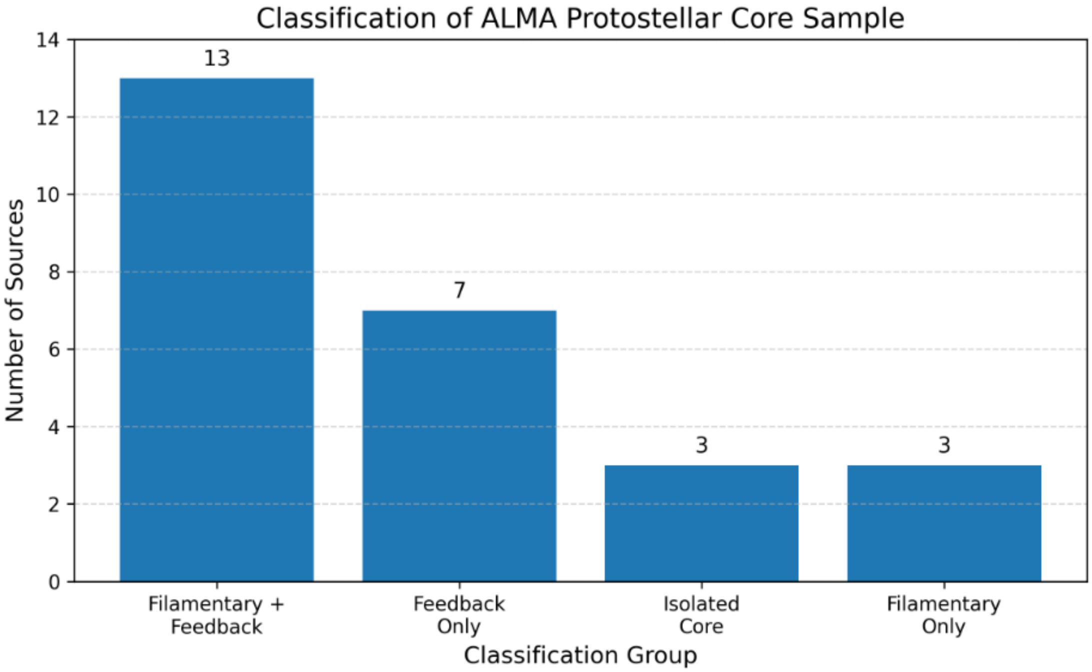

Figure 1: Distribution of the 26 ALMA protostellar cores across structural and feedback classification groups. The majority of sources are associated with both filamentary environments and active protostellar feedback, while a smaller fraction consists of isolated cores or filamentary systems without clear feedback signatures. This distribution indicates that most protostellar cores in the sample are embedded in dynamically evolving environments

Overall, the classification distribution demonstrates that core-scale star formation is typically associated with a combination of gas accretion and feedback processes. This provides a suitable framework for examining how magnetic field properties and star formation efficiency vary across different protostellar environments within a consistent physical regime.

Magnetic Field Strength and Star Formation Efficiency

The complete set of derived magnetic field strengths and SFE for the 26 ALMA protostellar cores is presented in Appendix Table A1. Figure 2 shows the distribution of plane-of-sky magnetic field strength, $\left(B_{pos}\right)$ as a function of SFE for the sample. The dataset spans over an order of magnitude in magnetic field strength, with (B_{pos}) ranging approximately from $(\sim 10^{-6})$ to

($\sim 10^{-3}$)G, while the star formation efficiency extends from ($\sim 10^{-2}$) to near unity. The distribution exhibits significant scatter, and no single monotonic or tight power-law relationship is observed between magnetic field strength and SFE.

Despite this scatter, the data do not form a purely random distribution. Instead, the sources occupy a structured region of parameter space, with a tendency for higher SFE values to be associated with weaker or moderately ordered magnetic field strengths, while lower SFE values are more commonly found in sources with relatively stronger fields. This trend, however, is not uniform across the sample and shows considerable overlap between regions.

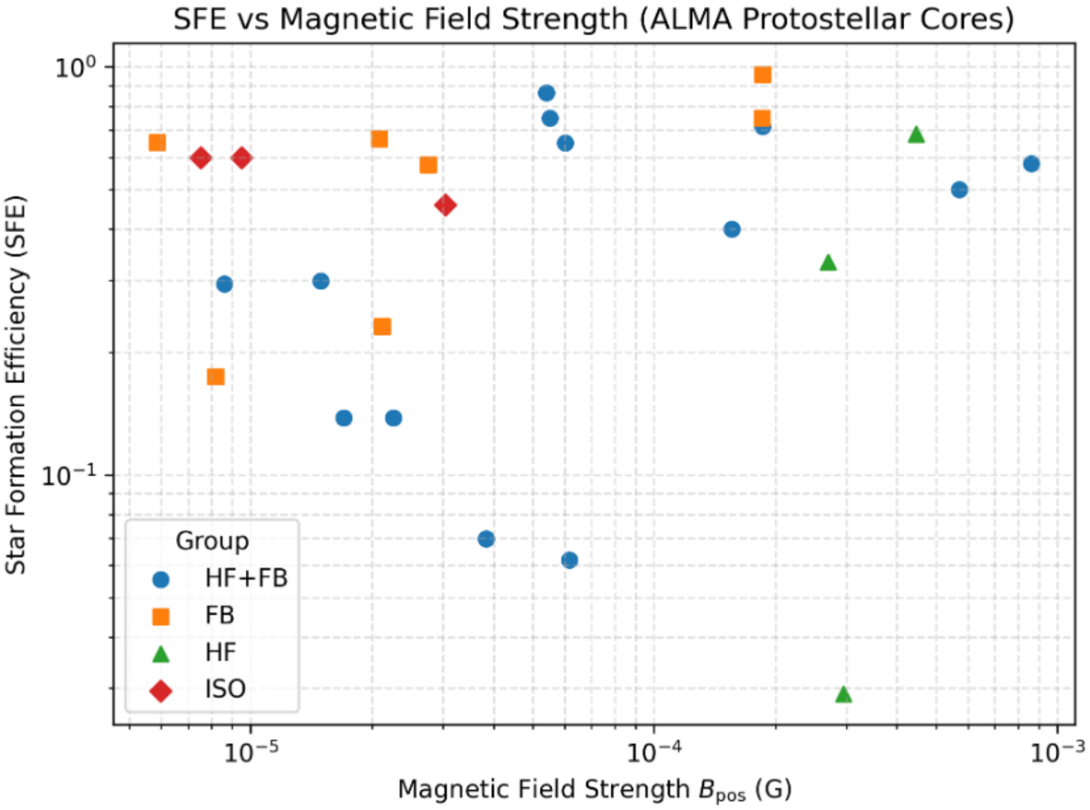

Figure 2: B_{pos} versus SFE for the 26 ALMA protostellar cores. Sources are grouped according to structural and feedback classification. The distribution shows significant scatter, with no single monotonic relationship between magnetic field strength and SFE. Instead, the data occupy a structured region of parameter space

Magnetic Field Morphology and Representative Source Properties

Each protostellar core in the ALMA sample was classified according to magnetic field morphology as hourglass, turbulent, or pinched, as described in Section 2.3. Representative sources illustrating these morphological classes, together with their magnetic field strengths and star formation efficiencies, are listed in Table 4, while the complete dataset is provided in Appendix Table A1.

Table 4: Magnetic Field Morphology, Field Strength, and SFE for Representative ALMA Protostellar Cores

Source	Morphology	B_{pos} (G)	SFE
L1448 IRS 2	Hourglass	6.16E-05	6.19E-02
HH 211 mm	Turbulent	5.87E-06	6.53E-01
SVS 13	Turbulent	1.86E-04	7.15E-01
CB 26	Turbulent	3.04E-05	4.59E-01
Ser-emb 6	Pinched	3.84E-05	6.98E-02
L1527	Hourglass	5.41E-05	8.66E-01

Table 4 highlights the characteristic differences between the morphological classes within protostellar core environments. Sources exhibiting hourglass magnetic field configurations, such as L1448 IRS 2, tend to be associated with relatively stronger and more ordered magnetic fields and moderate star formation efficiencies. In contrast, sources with turbulent magnetic fields, including HH 211 mm and SVS 13, display more disordered field structures and extend toward higher SFE values. Sources with pinched morphologies, such as Seremb 6, occupy intermediate positions in both magnetic field strength and efficiency.

These trends are further illustrated in Figure 3, which shows the distribution of all 26 ALMA protostellar cores grouped by morphology. While the three morphological classes overlap in parameter space, they occupy preferential regions: hourglass systems are more commonly found at relatively higher field strengths and moderate efficiencies; turbulent systems span a broader range and extend toward higher efficiencies; and pinched systems lie between these regimes.

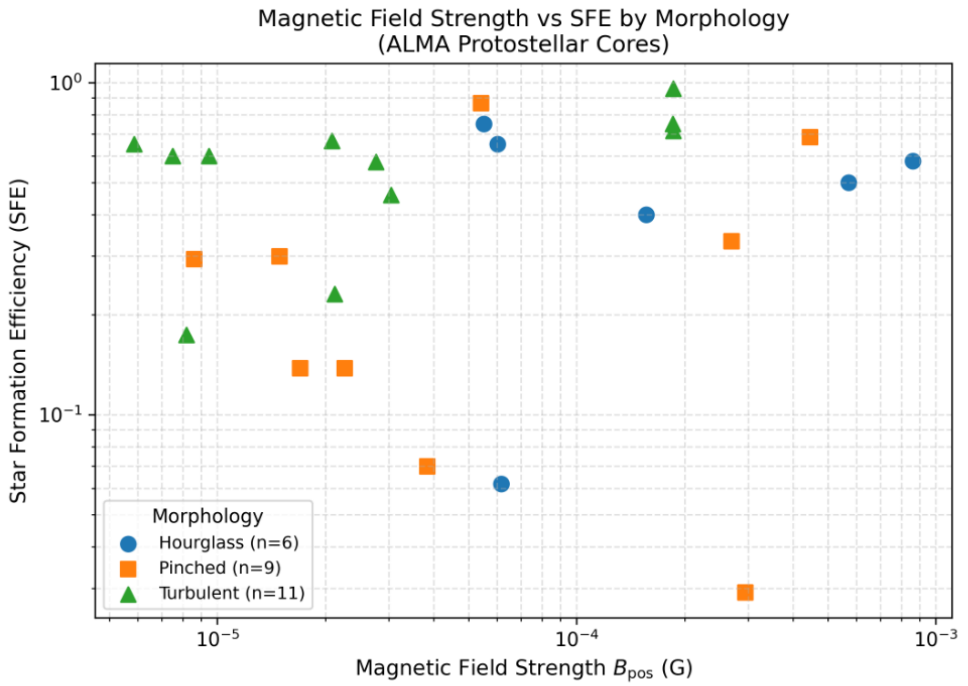

Figure 3: B_{pos} versus SFE for the 26 ALMA protostellar cores, grouped by magnetic field morphology. Hourglass, pinched, and turbulent field configurations occupy overlapping but distinct regions of parameter space. Hourglass morphologies tend to be associated with relatively stronger magnetic fields and moderate efficiencies, while turbulent morphologies extend toward higher SFE values. Pinched structures lie between these regimes. The overlap indicates that morphology influences, star formation efficiency at core scales

The consistency between the representative values listed in Table 4 and the full distribution shown in Figure 3 indicates that magnetic field morphology contributes systematically to the diversity of star formation efficiencies at protostellar core scales. However, similar to the trends observed in Section 4.2, morphology does not impose a single deterministic relationship between magnetic field strength and star formation efficiency.

Discussion

Magnetic Field Strength and Star Formation Efficiency

The results presented in Section 4.2 (Figure 2) show that the relationship between magnetic field strength and star formation efficiency (SFE) is not described by a simple monotonic or power-law correlation at protostellar core scales. Instead, the data exhibit a broad but structured distribution spanning over an order of magnitude in magnetic field strength and extending to near-unity SFE values. Although significant scatter is present, the distribution is not random. Sources with relatively weaker or moderately ordered magnetic fields tend to extend toward higher SFE values, while sources with stronger fields are more frequently associated with moderate efficiencies, although, with substantial overlap between regimes.

This behaviour is consistent with earlier observational and theoretical studies which suggest that magnetic fields influence, but do not uniquely regulate, star formation.

For example, Crutcher (2012) demonstrated that while magnetic field strength correlates with gas density on large scales, it alone cannot account for the efficiency of star formation. The absence of a tight global correlation in the present work confirms that this non-deterministic role of magnetic fields persists down to protostellar core scales.

Similarly, interferometric polarimetric observations by Hull (2014, 2017) and collaborators revealed significant diversity in magnetic field configurations within protostellar systems, indicating that turbulence and local dynamics can compete with magnetic regulation. However, those studies did not establish a statistical link with SFE. The present analysis extends these works by demonstrating that, although magnetic field strength alone does not define star formation efficiency, it contributes to a structured parameter space when considered alongside morphology and environmental conditions.

These findings therefore support a framework in which magnetic fields act as an important, but non-dominant, regulator of star formation at core scales.

Role of Magnetic Field Morphology

Magnetic field morphology provides further insight into the regulation of star formation at protostellar core scales. As shown in Figure 3 and summarized in Table 4, different morphological classes occupy partially distinct regions of the magnetic field strength-SFE parameter space.

Hourglass magnetic field configurations are generally associated with relatively stronger and more ordered fields and tend to exhibit moderate star formation efficiencies. These morphologies are widely interpreted as signatures of magnetically regulated gravitational collapse, in which field lines are compressed and aligned by infalling material. This interpretation is consistent with theoretical expectations that strong magnetic fields can slow collapse and regulate angular momentum transport, as discussed by Li et al. (2014) and collaborators.

In contrast, turbulent or disordered magnetic field morphologies extend toward higher SFE values and exhibit a broader distribution in parameter space. This suggests that reduced magnetic coherence allows gravity and local gas dynamics to dominate, leading to more efficient star formation in some regions. Observational studies of magnetic field structure evolution (e.g., Pattle et al. 2017, 2022) have similarly shown that magnetic fields can become increasingly disordered in dynamically active environments.

Pinched morphologies occupy intermediate positions, consistent with transitional states between ordered and disordered magnetic configurations. The classification scheme adopted here follows earlier morphological frameworks developed by Koch et al. (2012, 2018), but extends them by linking morphology directly to star formation efficiency across a statistically meaningful sample.

The overlap between morphological classes indicates that morphology influences, but does not uniquely determine, the efficiency of star formation. Instead, it reflects the dynamical state of the core and its interaction with magnetic fields and gas motions.

Influence of Structural Context and Feedback

The classification analysis (Section 4.1) shows that most protostellar cores in the sample are associated with filamentary environments and exhibit active feedback in the form of protostellar outflows and jets. These processes introduce additional complexity into the relationship between magnetic fields and star formation efficiency.

Filamentary structures are commonly interpreted as channels for mass accretion onto protostellar cores, as described in the filamentary star formation paradigm proposed by Myers (2009) and further developed by André et al. (2014). The broad distribution of SFE values observed among filamentary systems in the present sample indicates that accretion can proceed efficiently across a range of magnetic field conditions.

At the same time, feedback processes such as jets and outflows can perturb magnetic field geometry, redistribute gas, and modify collapse dynamics. Theoretical studies by Krumholz et al. (2014) and Dale (2015) have shown that feedback can both suppress and enhance star formation, depending on local conditions. The coexistence of filamentary accretion and feedback in many of the observed systems likely contributes to the dispersion in SFE and the absence of a simple magnetic field–efficiency relation.

These results therefore suggest that star formation efficiency at core scales is governed by a balance between accretion, magnetic support, turbulence, and feedback-driven gas redistribution.

Implications for Star Formation at Core Scales

Taken together, the results indicate that star formation efficiency in protostellar cores is not governed by a single controlling parameter, but instead arises from the interplay between magnetic fields, gas dynamics, structural environment, and feedback processes.

The observational trends identified in Figures 2 and 3 suggest that strong and ordered magnetic fields can moderate collapse, while weaker or more disordered configurations allow higher efficiencies. However, the significant overlap between different regimes demonstrates that magnetic regulation is neither uniform nor deterministic. This conclusion is consistent with modern theoretical frameworks of star formation, which emphasize the coupled roles of gravity, turbulence, and magnetic fields in shaping the evolution of molecular clouds.

Overall, the present study provides observational evidence that magnetic fields influence, but do not uniquely control, star formation efficiency at protostellar core scales.

CONCLUSION

We have presented a comparative observational analysis of magnetic field morphology and star formation efficiency in a sample of 26 low-mass protostellar cores observed with ALMA polarimetric data. The study investigated how magnetic-field strength, morphology, structural environment, and feedback activity relate to star formation efficiency at protostellar core scales within a homogeneous interferometric framework.

The results show that magnetic-field strengths span more than an order of magnitude, while star formation efficiencies range from moderate to high values. No single monotonic relationship was found between magnetic-field strength and star formation efficiency, indicating that magnetic fields do not uniquely regulate star formation at core scales. Instead, the observed distributions reveal a structured parameter space in which magnetic-field morphology and local environmental conditions contribute significantly to the diversity of star formation outcomes.

Hourglass magnetic-field morphologies are generally associated with relatively stronger and more ordered fields and tend to exhibit moderate efficiencies, consistent with magnetically regulated collapse. In contrast, turbulent morphologies extend toward higher star formation efficiencies and display broader parameter distributions, suggesting that local gas dynamics and reduced magnetic coherence can enhance collapse activity. Pinched morphologies occupy intermediate regimes between ordered and turbulent configurations.

The classification analysis further shows that most protostellar cores in the sample are associated with filamentary environments and active protostellar feedback, indicating that accretion and feedback processes commonly coexist during core evolution. These processes likely contribute to the observed dispersion in star formation efficiency and reinforce the conclusion that magnetic regulation operates together with turbulence, gas inflow, and feedback-driven redistribution of material.

Overall, this study provides observational evidence that magnetic fields influence, but do not solely determine, star formation efficiency in low-mass protostellar cores. The results highlight the importance of considering magnetic-field geometry together with environmental and dynamical processes in understanding the evolution of star-forming regions.

ACKNOWLEDGMENTS

We acknowledge the use of data from the Atacama Large Millimeter/submillimeter Array science archive. ALMA is a partnership of ESO (representing its member states), NSF (USA), and NINS (Japan), together with NRC (Canada), MOST and ASIAA (Taiwan), and KASI (Republic of Korea), in cooperation with the Republic of Chile. This research has also made use of NASA's Astrophysics Data System (ADS). We are grateful to Prof. Jemima N. Ogwo for her great contribution and guidance, and to Prof. I. U. Chiemeka and Dr. E. C. Nwaokoro of Abia State University, Uturu, Nigeria, for their constructive comments and encouragement.

REFERENCES

André, P., Men'shchikov, A., Bontemps, S., Könyves, V., Motte, F., Schneider, N., Didelon, P., Minier, V., Saraceno, P., Ward-Thompson, D., di Francesco, J., White, G., Molinari, S., Testi, L., Abergel, A., Griffin, M., Henning, T., Royer, P., Merín, B., Vavrek, R., et al. (2010). From filamentary clouds to prestellar cores to the stellar IMF: Initial highlights from the Herschel Gould Belt Survey. *Astronomy & Astrophysics*, 518*, L102*. https://doi.org/10.1051/0004-6361/201014666

André, P., Men'shchikov, A., Bontemps, S., Könyves, V., Motte, F., Schneider, N., Didelon, P., Minier, V., Saraceno, P., Ward-Thompson, D., di Francesco, J., White, G., Molinari, S., Testi, L., Abergel, A., Griffin, M., Henning, T., Royer, P., Merín, B., Vavrek, R., et al. (2010). From filamentary clouds to prestellar cores to the stellar IMF: Initial highlights from the Herschel Gould Belt Survey. *Astronomy & Astrophysics*, 518*, L102*. https://doi.org/10.1051/0004-6361/201014666

Arce, H. G., Shepherd, D., Gueth, F., Lee, C.-F., Bachiller, R., Rosen, A., & Beuther, H. (2007). Molecular outflows in low- and high-mass star-forming regions. In B. Reipurth, D. Jewitt, & K. Keil (Eds.), **Protostars and planets V** (*pp. 245– 260*). *University of Arizona Press*.

Bakare, H. O., Chukwuma, V. U., & Adekoya, B. J. (2024). Inter-Correlation Analysis of Magnetic Activity Indices during Varying Geomagnetic Conditions and Phases. Nigerian Journal of Physics, 33(1), 152-171. https://doi.org/10.62292/njp.v33i1.2024.210

Bally, J. (2016). Protostellar outflows. *Annual Review of *Astronomy and Astrophysics*, 54*, 491–528*. https://doi.org/10.1146/annurev-astro-081915-023341

Brand, J., Massi, F., & Giannini, T. (2019). Star formation in molecular clouds. **Astronomy & Astrophysics*, 626*, A86. https://doi.org/10.1051/0004-6361/201935354

Chandrasekhar, S., & Fermi, E. (1953). Magnetic fields in spiral arms. **The Astrophysical Journal*, 118*, 113–115*. https://doi.org/10.1086/145732

Chen, X., Launhardt, R., & Henning, T. (2009). Structure and evolution of protostellar cores. **The Astrophysical Journal*, 695*(1), 511–522*. https://doi.org/10.1088/0004-637X/695/1/511

Chiang, H.-F., Looney, L. W., & Tobin, J. J. (2010). Protostellar disk evolution in embedded systems. **The Astrophysical Journal*, 709*(1), 470–482*. https://doi.org/10.1088/0004-637X/709/1/470

Chiang, H.-F., Looney, L. W., Tobin, J. J., & Hartmann, L. (2012). Protostellar collapse and disk structures. **The Astrophysical Journal*, 756*(2), 168*. https://doi.org/10.1088/0004-637X/756/2/168

Crutcher, R. M. (2012). Magnetic fields in molecular clouds. **Annual Review of Astronomy and Astrophysics*, 50*, 29–63*. https://doi.org/10.1146/annurev-astro-081811-125514

Crutcher, R. M., Nutter, D. J., Ward-Thompson, D., & Kirk, J. M. (2004). Magnetic field measurements in molecular clouds. **The Astrophysical Journal*, 600*(1), 279–285*. https://doi.org/10.1086/379705

Dale, J. E. (2015). Ionizing feedback from massive stars in massive clusters. **New Astronomy Reviews*, 68*, 1–33*. https://doi.org/10.1016/j.newar.2015.05.001

Davis, L. (1951). The strength of interstellar magnetic fields. **Physical Review*, 81*(5), 890–891*. https://doi.org/10.1103/PhysRev.81.890

Dutrey, A., Guilloteau, S., & Simon, M. (1996). Circumstellar disks around young stellar objects. **Astronomy & Astrophysics*, 309*, 493–504*.

Enoch, M. L., Evans, N. J., Sargent, A. I., et al. (2009). Properties of protostellar cores in nearby molecular clouds. **The Astrophysical Journal*, 692*(2), 973– 997*. https://doi.org/10.1088/0004-637X/692/2/973

Evans, N. J., Dunham, M. M., Jørgensen, J. K., et al. (2009). The Spitzer c2d legacy results. **The Astrophysical Journal Supplement Series*, 181*(2), 321–350*. https://doi.org/10.1088/0067-0049/181/2/321

Frank, A., Ray, T. P., Cabrit, S., et al. (2014). Jets and outflows from star to cloud. In H. Beuther, R. S. Klessen, C. P. Dullemond, & T. Henning (Eds.), **Protostars and planets VI** (*pp. 451–474*). *University of Arizona Press*.

Gaia Collaboration, Brown, A. G. A., Vallenari, A., et al. (2018). Gaia Data Release 2. **Astronomy & Astrophysics*, 616*, A1*. https://doi.org/10.1051/0004-6361/201833051

Girart, J. M., Rao, R., & Marrone, D. P. (2006). Magnetic fields in star-forming regions. **Science*, 313*(5788), 812–814*. https://doi.org/10.1126/science.1129092

Hartmann, L., Megeath, S. T., Allen, L., et al. (2005). Star formation in the Taurus molecular cloud. **The Astrophysical Journal*, 629*(2), 881–896*. https://doi.org/10.1086/431472

Henning, T., Launhardt, R., & Stecklum, B. (2001). Dust properties in protostellar environments. **The Astrophysical Journal Letters*, 561*(1), L89–L92*. https://doi.org/10.1086/324381

Hildebrand, R. H. (1983). The determination of cloud masses and dust characteristics from submillimetre thermal emission. **Quarterly Journal of the Royal Astronomical Society*, 24*, 267–282*.

Hildebrand, R. H., Kirby, L., Dotson, J. L., et al. (2009). Dispersion of magnetic fields in molecular clouds. **The Astrophysical Journal*, 696*(1), 567–573*. https://doi.org/10.1088/0004-637X/696/1/567

Houde, M., Vaillancourt, J. E., Hildebrand, R. H., et al. (2009). Dispersion analysis of magnetic fields. **The Astrophysical Journal*, 706*(2), 1504–1516*. https://doi.org/10.1088/0004-637X/706/2/1504 Hull, C. L. H., Plambeck, R. L., Kwon, W., et al. (2014). Misalignment of magnetic fields and outflows in protostellar cores. **The Astrophysical Journal Supplement Series*, 213*(1), 13*. https://doi.org/10.1088/0067-0049/213/1/13

Hull, C. L. H., Girart, J. M., Tychoniec, Ł., et al. (2017a). ALMA polarization observations of protostellar systems. **The Astrophysical Journal Letters*, 842*(1), L9*. https://doi.org/10.3847/2041-8213/aa71b7

Hull, C. L. H., Girart, J. M., Tychoniec, Ł., et al. (2017b). Magnetic fields in protostellar envelopes. **The Astrophysical Journal*, 847*(2), 92*. https://doi.org/10.3847/1538-4357/aa7fe9

Hull, C. L. H., & Zhang, Q. (2019). Magnetic fields in low-mass star formation. **Frontiers in Astronomy and Space Sciences*, 6*, 3*. https://doi.org/10.3389/fspas.2019.00003

Kauffmann, J., Bertoldi, F., Bourke, T. L., et al. (2008). Low-mass star formation and dense cores in molecular clouds. *Astronomy & Astrophysics*, *487*(3), 993– 1008.* https://doi.org/10.1051/0004-6361:200809481

Koch, P. M., Tang, Y.-W., & Ho, P. T. P. (2012). Magnetic field structures in collapsing protostellar cores. **The Astrophysical Journal*, *747*(1), 79.* https://doi.org/10.1088/0004-637X/747/1/79

Koch, P. M., Tang, Y.-W., & Ho, P. T. P. (2018). Magnetic field morphology in star- forming regions. **The Astrophysical Journal*, *855*(1), 39.* https://doi.org/10.3847/1538-4357/aaa4cf

Krumholz, M. R., Bate, M. R., Arce, H. G., et al. (2014). The formation of stellar clusters and massive stars. In H. Beuther, R. S. Klessen, C. P. Dullemond, & T. Henning (Eds.), **Protostars and planets VI** (*pp. 243–266*). *University of Arizona Press.*

Launhardt, R., & Sargent, A. I. (2001). Compact circumstellar structures in protostellar systems. **The Astrophysical Journal Letters*, *562*(2), L173–L176.* https://doi.org/10.1086/338252

Launhardt, R., Ward-Thompson, D., & Henning, T. (2000). Prestellar core properties in nearby molecular clouds. **The Astrophysical Journal Supplement Series*, *127*(1), 129–146.* https://doi.org/10.1086/313313

Lee, C.-F., Hirano, N., Palau, A., et al. (2009). Protostellar jets and outflows in young stellar objects. **The Astrophysical Journal*, *699*(2), 1584–1594.* https://doi.org/10.1088/0004-637X/699/2/1584

Lee, C.-F., Rao, R., Ching, T.-C., et al. (2014). Magnetic fields and protostellar collapse. **The Astrophysical Journal*, *797*(1), L9.* https://doi.org/10.1088/2041-8205/797/1/L9

Li, H.-B., Goodman, A., Sridharan, T. K., et al. (2014). The role of magnetic fields in molecular cloud and star formation. In H. Beuther, R. S. Klessen, C. P. Dullemond, & T. Henning (Eds.), **Protostars and planets VI** (*pp. 101–123*). University of Arizona Press.

Liu, J., Qiu, K., Zhang, Q., et al. (2021). Magnetic field structures in protostellar cores observed with ALMA. **The Astrophysical Journal Supplement Series*, *253*(1), 14.* https://doi.org/10.3847/1538-4365/abd5c8

Looney, L. W., Mundy, L. G., & Welch, W. J. (2000). Unveiling circumstellar structures in embedded protostars. **The Astrophysical Journal*, *529*(1), 477–498.* https://doi.org/10.1086/308239

Massi, F., Testi, L., Brand, J., et al. (2008). Star formation activity in molecular clouds. **Astronomy & Astrophysics*, *490*(3), 1079–1090.* https://doi.org/10.1051/0004-6361:200810036

McKee, C. F., & Ostriker, E. C. (2007). Theory of star formation. **Annual Review of Astronomy and Astrophysics*, *45*, 565–687.* https://doi.org/10.1146/annurev.astro.45.051806.110602

Motte, F., Bontemps, S., & Louvet, F. (2018). High-mass star and massive cluster formation in the Milky Way. **Annual Review of Astronomy and Astrophysics*, *56*, 41–82.* https://doi.org/10.1146/annurev-astro-091916-055235

Murillo, N. M., & Lai, S.-P. (2013). Magnetic field structures in protostellar envelopes. **The Astrophysical Journal Letters*, *764*(1), L15–L20.* https://doi.org/10.1088/2041-8205/764/1/L15

Murillo, N. M., Lai, S.-P., Bruderer, S., et al. (2013). Embedded protostellar disk formation and structure. **Astronomy & Astrophysics*, *560*, A103.* https://doi.org/10.1051/0004-6361/201322537

Myers, P. C. (2009). Filamentary structure and cluster formation in molecular clouds. **The Astrophysical Journal, 700*(2), 1609–1619.* https://doi.org/10.1088/0004-637X/700/2/1609

Ochsenbein, F., Bauer, P., & Marcout, J. (2000). The VizieR database of astronomical catalogues. **Astronomy and Astrophysics Supplement Series*, *143*(1), 23–32.* https://doi.org/10.1051/aas:2000169

Okezuonu, P. C., & Ogwo, J. N. (2021). Density dependence of star formation efficiency in Galactic star-forming regions. **International Journal of Astrophysics and Space Science*, *9*(1), 12–18.* https://doi.org/10.11648/j.ijass.20210901.12

Ostriker, E. C., Stone, J. M., & Gammie, C. F. (2001). Density, velocity, and magnetic field structure in turbulent molecular cloud models. **The Astrophysical Journal*, *546*(2), 980–1005.* https://doi.org/10.1086/318290

Planck Collaboration Int. XXXV. (2016). Probing the role of the magnetic field in the formation of structure in molecular clouds. **Astronomy & Astrophysics*, *586*, A138.* https://doi.org/10.1051/0004-6361/201425273

Pattle, K., Ward-Thompson, D., Berry, D., et al. (2017). The JCMT BISTRO survey: Magnetic fields within the

Ophiuchus molecular cloud. *The Astrophysical Journal, 846*(2), 122–141. https://doi.org/10.3847/1538-4357/aa8096

Pattle, K., Ward-Thompson, D., Lai, S.-P., et al. (2022). Magnetic field evolution in nearby star-forming regions. *The Astrophysical Journal, 927*(1), 12–30. https://doi.org/10.3847/1538-4357/ac4651

Pattle, K., Ward-Thompson, D., Soam, A., et al. (2023). Magnetic fields in nearby molecular clouds from the BISTRO survey. *Astronomy & Astrophysics, 671*, A115. https://doi.org/10.1051/0004-6361/202244806

Sandell, G., & Knee, L. B. G. (2001). Dust emission and embedded protostars in molecular clouds. *The Astrophysical Journal Letters, 546*(1), L49–L52. https://doi.org/10.1086/318871

Saito, M., Sunada, K., Kawabe, R., et al. (1999). Dense molecular gas and star formation activity in protostellar regions. *The Astrophysical Journal, 518*(1), 334–343. https://doi.org/10.1086/307258

Soam, A., Ward-Thompson, D., Pattle, K., et al. (2018). Magnetic field morphology in dense star-forming filaments. *The Astrophysical Journal, 861*(1), 65–78. https://doi.org/10.3847/1538-4357/aac4be

Stephens, I. W., Looney, L. W., Kwon, W., et al. (2013). Magnetic field structure in protostellar systems observed with CARMA. *The Astrophysical Journal Letters, 769*(1), L15. https://doi.org/10.1088/2041-8205/769/1/L15

Stutz, A. M., Rubin, M., Werner, M. W., et al. (2008). Embedded protostars and dense cores in molecular clouds. *The Astrophysical Journal, 687*(1), 389– 401. https://doi.org/10.1086/591789

Stutz, A. M., Launhardt, R., Linz, H., et al. (2010). The Herschel view of star-forming regions in Aquila. *Astronomy & Astrophysics, 518*, L87. https://doi.org/10.1051/0004-6361/201014667

Takakuwa, S., Saito, M., Lim, J., et al. (2012). Protostellar disk and envelope structures in Class I systems. *The Astrophysical Journal, 754*(1), 52–66. https://doi.org/10.1088/0004-637X/754/1/52

Takakuwa, S., Saito, M., Lim, J., et al. (2014). Rotating protostellar envelopes and disk growth. *The Astrophysical Journal, 796*(1), 1–17. https://doi.org/10.1088/0004-637X/796/1/1

Tobin, J. J., Hartmann, L., Chiang, H.-F., et al. (2010). Protostellar binary formation and circumstellar structures. *The Astrophysical Journal, 712*(2), 1010–1026. https://doi.org/10.1088/0004-637X/712/2/1010

Tobin, J. J., Hartmann, L., Chiang, H.-F., et al. (2012a). A 100 AU protostellar disk around a Class 0 source. *Nature, 492*(7427), 83–85. https://doi.org/10.1038/nature11610

Tobin, J. J., Hartmann,L., Chiang, H.-F., et al. (2012b). Circumstellar structures in embedded protostars. *The Astrophysical Journal, 748*(1), 16. https://doi.org/10.1088/0004-637X/748/1/16

Tobin, J. J., Looney, L. W., Li, Z.-Y., et al. (2013). Disk formation in embedded protostars. *The Astrophysical Journal, 771*(1), 48. https://doi.org/10.1088/0004-637X/771/1/48

Tobin, J. J., Looney, L. W., Li, Z.-Y., et al. (2016). The VANDAM survey of protostellar disks. *The Astrophysical Journal, 818*(1), 73. https://doi.org/10.3847/0004-637X/818/1/73

Urquhart, J. S., König, C., Giannetti, A., et al. (2018). ATLASGAL—Properties of dense clumps associated with high-mass star formation. *Monthly Notices of the Royal Astronomical Society, 473*(1), 1059–1078. https://doi.org/10.1093/mnras/stx2258

Ward-Thompson, D., Pattle, K., Kirk, J. M., et al. (2017). First results from the BISTRO survey of the Gould Belt. *The Astrophysical Journal, 842*(2), 66. https://doi.org/10.3847/1538-4357/aa71b2

Wolf-Chase, G. A., Arvidsson, K., & Smutko, M. (2003). Star formation and molecular gas structure in dense clouds. *The Astronomical Journal, 126*(3), 1307–1322. https://doi.org/10.1086/377070

Yen, H.-W., Takakuwa, S., & Ohashi, N. (2010). Protostellar collapse and envelope kinematics. *The Astrophysical Journal, 710*(2), 1786–1797. https://doi.org/10.1088/0004-637X/710/2/1786

Yen, H.-W., Takakuwa, S., Ohashi, N., et al. (2015). Magnetic braking and disk formation in protostellar systems. *The Astrophysical Journal, 799*(2), 193. https://doi.org/10.1088/0004-637X/799/2/193

Zinnecker, H., & Yorke, H. W. (2007). Toward understanding massive star formation. *Annual Review of Astronomy and Astrophysics, 45*, 481–563. https://doi.org/10.1146/annurev.astro.44.051905.092549

Appendix

Table A1: Full Catalog of Star-Forming Regions

S/N	Source	d (pc)	H–F	FB	Classification Group	Morphology	Bpos, DCF (μG)	Bpos, (G)	$M_\star$ ($M_\odot$)	Gas Mass ($M_\odot$)	SFE
3	L1448 IRS 2	293	Yes	Yes	Low-Mass + HF + FB	Hourglass	61.64	6.164E-5	1.65	25	6.19E-02
4	L1448N(B)	293	Yes	Yes	Low-Mass + HF + FB	Hourglass	55.05	5.505E-5	1.5	0.5	7.50E-01
5	L1448C	293	Yes	Yes	Low-Mass + HF + FB	Hourglass	60.26	6.026E-5	1.5	0.8	6.52E-01
6	L1455 IRS 1	293	Yes	No	Low-Mass + HF	Pinched	445.83	4.4583E-4	1.3	0.6	6.84E-01
7	NGC 1333–IRAS 2A	293	Yes	No	Low-Mass + HF	Pinched	294.91	2.9491E-4	1.5	50	2.91E-02
8	NGC 1333–IRAS 4A	293	Yes	Yes	Low-Mass + HF + FB	Hourglass	156.36	1.5636E-4	1.93	2.9	4.00E-01
9	NGC 1333–IRAS 4B	293	Yes	Yes	Low-Mass + HF + FB	Hourglass	862.15	8.6215E-4	1.38	1	5.80E-01
10	NGC 1333–IRAS 4B2	293	Yes	Yes	Low-Mass + HF + FB	Hourglass	570.83	5.7083E-4	1.5	1.5	5.00E-01
11	SVS 13	293	Yes	Yes	Low-Mass + HF + FB	Turbulent	185.87	1.8587E-4	2.51	1	7.15E-01
12	HH 211 mm	293	No	Yes	Low-Mass + FB	Turbulent	5.87	5.87E-6	1.41	0.75	6.53E-01
13	DG Tau	140	No	Yes	Low-Mass + FB	Turbulent	185.86	1.8586E-4	1.19	0.05	9.60E-01
14	L1551 NE	140	No	Yes	Low-Mass + FB	Turbulent	184.75	1.8475E-4	1.5	0.5	7.50E-01
15	L1527	140	Yes	Yes	Low-Mass + HF + FB	Pinched	54.12	5.412E-5	1.29	0.2	8.66E-01
16	CB 26	140	No	No	Low-Mass	Turbulent	30.39	3.039E-5	0.85	1	4.59E-01
23	VLA 1623	125	No	Yes	Low-Mass + FB	Turbulent	20.82	2.082E-5	1	0.5	6.67E-01
24	Ser-emb 17	436	Yes	Yes	Low-Mass + HF + FB	Pinched	8.62	8.62E-6	1.5	3.6	2.94E-01
25	Ser-emb 1	436	Yes	Yes	Low-Mass + HF + FB	Pinched	14.92	1.492E-5	1.32	3.1	2.99E-01
26	Ser-emb 8	436	Yes	Yes	Low-Mass + HF + FB	Pinched	22.62	2.262E-5	1.5	9.4	1.38E-01
27	Ser-emb 8 (N)	436	Yes	Yes	Low-Mass + HF + FB	Pinched	16.97	1.697E-5	1.5	9.4	1.38E-01
28	Ser-emb 6	436	Yes	Yes	Low-Mass + HF + FB	Pinched	38.4	3.84E-5	1.5	20.0	6.98E-02
29	HH 108 IRAS	310	No	Yes	Low-Mass + FB	Turbulent	21.23	2.123E-5	1.5	5.0	2.31E-01
32	B335 IRS	150	No	Yes	Low-Mass + FB	Turbulent	8.19	8.19E-6	1.05	5	1.74E-01
34	L1157	325	No	Yes	Low-Mass + FB	Turbulent	27.56	2.756E-5	1.36	1	5.76E-01
35	CB 230	325	Yes	No	Low-Mass + HF	Pinched	269.90	2.699E-4	1.5	3	3.33E-01
36	L1165	300	No	No	Low-Mass	Turbulent	9.48	9.48E-6	1.5	1	6.00E-01
38	CB 244	200	No	No	Low-Mass	Turbulent	7.51	7.51E-6	1.5	1	6.00E-01

Note: Source - Name of the star-forming region, Mass Class - Low-mass or High-mass, Hub–Filament (H-F) - Presence (Yes) or absence (No) of a hub–filament system, Feedback (FB) - Presence (Yes) or absence (No) of stellar feedback, Classification Group - Combined environmental category, B_{pos}- Plane-of-sky magnetic field strength in microgauss, $M_\star$ - Stellar mass in solar masses and SFE - Star-formation efficiency. Also note that The star-formation efficiencies were computed uniformly for all sources using $SFE = M_\star/M_\star + M_{gas}$. This correction removed earlier spreadsheet inconsistencies and ensured that all SFE values lie within the physically meaningful interval $0 < SFE < 1$.

Table A2: Input Parameters and Validity Assessment for DCF Magnetic Field Estimates

S/N	Source	$\rho(gcm^{-3})$	σ_v (kms^{-1})	$\sigma_\phi(deg)$	$\sigma_\phi(rad)$	$B_{pos}cal$ (μG)	DCF validity note
1	L1448 IRS 2	3.32E-19	1.50	43	0.7505	61.64	caution
2	L1448N(B)	1.69E-18	0.60	37	0.6458	55.05	caution
3	L1448C	1.68E-18	0.70	32	0.5585	60.26	caution
4	L1455 IRS 1	5.84E-19	0.50	24	0.4189	445.83	valid
5	NGC 1333-IRAS 2A	1.67E-18	1.50	23	0.4014	294.91	valid
6	SVS 13	1.67E-18	1.50	24	0.4189	156.36	valid
7	NGC 1333-IRAS 4A	3.34E-17	2.00	20	0.3491	862.15	valid
8	NGC 1333-IRAS 4B	9.35E-18	2.00	34	0.5934	570.83	caution
9	NGC 1333-IRAS 4B2	4.68E-18	1.00	20	0.3491	185.87	valid
10	HH 211 mm	2.41E-21	0.70	32	0.5585	5.87	caution
11	DG Tau	3.35E-19	2.00	14	0.2443	185.86	valid
12	L1551 NE	3.55E-18	1.50	15	0.2618	184.75	valid
13	L1527	3.35E-19	0.35	08	0.1396	54.12	Valid
14	CB 26	3.35E-19	0.50	66	1.1519	30.39	caution
15	VLA 1623	6.46E-20	1.00	48	0.8378	20.82	caution
16	Ser-emb 17	6.46E-20	0.50	39	0.6807	8.62	caution
17	Ser-emb 1	1.29E-19	0.50	52	0.9076	14.92	caution
18	Ser-emb 8	6.46E-20	0.50	44	0.7679	22.62	caution
19	Ser-emb 8 (N)	6.46E-20	0.50	15	0.2618	16.97	valid
20	Ser-emb 6	3.23E-19	0.50	33	0.5760	38.40	caution
21	HH 108 IRAS	8.06E-20	0.60	34	0.5934	21.23	caution
22	B335 IRS	8.06E-20	0.30	40	0.6981	8.19	caution
23	L1157	2.41E-20	2.00	29	0.5061	27.56	caution
24	CB 230	3.91E-20	5.00	35	0.6109	269.90	caution
25	L1165	1.30E-20	1.00	04	0.0698	9.48	valid
26	CB 244	1.30E-20	1.00	49	0.8552	7.51	caution

Notes: The plane-of-sky magnetic field strength was recalculated using the DCF relation $B_{pos} = 0.5\sqrt{4\pi\rho}(\sigma_v/\sigma_\phi)$, with $\sigma_\phi$converted from degrees to radians and σ_v converted from kms^{-1} to cms^{-1}. Magnetic-field strengths are reported to two significant figures only. The DCF method is considered valid for small angular dispersions $\sigma_\phi \geq 25^o$. Sources with $25^o < \sigma_\phi < 45^o$ are flagged as Caution, while those exceeding this range or with incomplete input parameters are labeled Limited. This table provides the full set of input parameters used in deriving magnetic field strengths and forms the basis for the analysis presented in Figures 2–4.

Table A3: Physical properties, environmental classification, corrected DCF magnetic-field strengths, star formation efficiencies, and morphology assignments for the 38-source sample

S/N	Source	Mass Class	d (pc)	H–F	FB	Classification Group	Bpos, DCF (microG)	Bpos, DCF (G)	SFE	Morphology
1	L1448 IRS 2	Low	293	Yes	Yes	Low-Mass + HF + FB	61.64	6.16E-05	6.19E-02	Hourglass
2	L1448N(B)	Low	293	Yes	Yes	Low-Mass + HF + FB	55.05	5.51E-05	7.50E-01	Hourglass
3	L1448C	Low	293	Yes	Yes	Low-Mass + HF + FB	60.26	6.03E-05	6.52E-01	Hourglass
4	L1455 IRS 1	Low	293	Yes	No	Low-Mass + HF	445.83	4.46E-04	6.84E-01	Pinched
5	NGC 1333–IRAS 2A	Low	293	Yes	No	Low-Mass + HF	294.91	2.95E-04	2.91E-02	Pinched
6	NGC 1333–IRAS 4A	Low	293	Yes	Yes	Low-Mass + HF + FB	156.36	1.56E-04	4.00E-01	Hourglass
7	NGC 1333–IRAS 4B	Low	293	Yes	Yes	Low-Mass + HF + FB	862.15	8.62E-04	5.80E-01	Hourglass
8	NGC 1333–IRAS 4B2	Low	293	Yes	Yes	Low-Mass + HF + FB	570.83	5.71E-04	5.00E-01	Hourglass
9	SVS 13	Low	293	Yes	Yes	Low-Mass + HF + FB	185.87	1.86E-04	7.15E-01	Turbulent
10	HH 211 mm	Low	293	No	Yes	Low-Mass + FB	5.87	5.87E-06	6.53E-01	Turbulent
11	DG Tau	Low	140	No	Yes	Low-Mass + FB	185.86	1.86E-04	9.60E-01	Turbulent
12	L1551 NE	Low	140	No	Yes	Low-Mass + FB	184.75	1.85E-04	7.50E-01	Turbulent
13	L1527	Low	140	Yes	Yes	Low-Mass + HF + FB	54.12	5.41E-05	8.66E-01	Pinched
14	CB 26	Low	140	No	No	Low-Mass	30.39	3.04E-05	4.59E-01	Turbulent
15	VLA 1623	Low	125	No	Yes	Low-Mass + FB	20.82	2.08E-05	6.67E-01	Turbulent
16	Ser-emb 17	Low	436	Yes	Yes	Low-Mass + HF + FB	8.62	8.62E-06	2.94E-01	Pinched
17	Ser-emb 1	Low	436	Yes	Yes	Low-Mass + HF + FB	14.92	1.49E-05	2.99E-01	Pinched
18	Ser-emb 8	Low	436	Yes	Yes	Low-Mass + HF + FB	22.62	2.26E-05	1.38E-01	Pinched
19	Ser-emb 8 (N)	Low	436	Yes	Yes	Low-Mass + HF + FB	16.97	1.70E-05	1.38E-01	Pinched
20	Ser-emb 6	Low	436	Yes	Yes	Low-Mass + HF + FB	38.4	3.84E-05	6.98E-02	Pinched
21	HH 108 IRAS	Low	310	No	Yes	Low-Mass + FB	21.23	2.12E-05	2.31E-01	Turbulent
22	B335 IRS	Low	150	No	Yes	Low-Mass + FB	8.19	8.19E-06	1.74E-01	Turbulent
23	L1157	Low	325	No	Yes	Low-Mass + FB	27.56	2.76E-05	5.76E-01	Turbulent
24	CB 230	Low	325	Yes	No	Low-Mass + HF	269.9	2.70E-04	3.33E-01	Pinched
25	L1165	Low	300	No	No	Low-Mass	9.48	9.48E-06	6.00E-01	Turbulent
26	CB 244	Low	200	No	No	Low-Mass	7.51	7.51E-06	6.00E-01	Turbulent

Notes: Bpos,DCF values are the corrected plane-of-sky magnetic-field strengths derived using the Davis–Chandrasekhar–Fermi method. Values in Gauss were obtained by converting µG to G using $1\mu G = 10^{-6}G$. Star formation efficiency was recomputed uniformly as $SFE = M_{\star}/(M_{\star} + M_{gas})$. Morphology classes were standardized as Hourglass, Pinched, and Turbulent for comparative analysis.